Geochemistry, Geophysics, Geosystems

RESEARCH ARTICLE
10.1029/2018GC007806

# A Geodetic Strain Rate and Tectonic Velocity Model for China

X. Rui[1] and D. S. Stamps[2]

[1]Sichuan Earthquake Bureau, Research Institute of Disaster Reduction and Emergency Rescue, Chengdu, China, [2]Department of Geosciences, Geodesy and Tectonophysics Laboratory, Virginia Tech, Blacksburg, VA, USA

**Key Points:**
- Tectonic velocity solution for China derived from Global Positioning System data spanning 1996-2017
- Using a novel checkerboard test, Bayesian statistics, and 2-D analytic shear strain rates, we develop a tectonic strain rate model for China
- Tectonic forecast model of shallow seismicity for mainland China shows increased seismic risk in the North China Block

**Supporting Information:**
- Supporting Information S1
- Data Set S1
- Data Set S2
- Data Set S3

**Correspondence to:**
X. Rui,
xurui_3@163.com

**Citation:**
Rui, X., & Stamps, D. S. (2019). A geodetic strain rate and tectonic velocity model for China. *Geochemistry, Geophysics, Geosystems*, *20*, 1280–1297. https://doi.org/10.1029/2018GC007806

Received 2 JUL 2018
Accepted 30 JAN 2019
Accepted article online 5 FEB 2019
Published online 1 MAR 2019



**Abstract** The conjoining and interfering influence of the Circum-Pacific zone and the Tethys-Himalayan zone make China a country of intense intracontinental seismicity. Here we provide three new quantitatively assessed products and use them to better constrain seismic hazards in China. First, we process ~2,700 Global Positioning System (GPS) data spanning 1996–2017 provided by the Crustal Movement Observation Network of China (CMONOC) network and the Nevada Geodetic Laboratory. To produce a robust tectonic velocity solution, we implement a data editing scheme to account for 8 Mw $\geq$ 7 earthquakes to reduce the influence of transient phenomena. The solution is then rotated into a consistent reference frame with 10 other published velocity sources surrounding mainland China. Second, we calculate a new geodetic strain rate model using an optimal mesh grid definition of 0.4° × 0.4° determined jointly by the Nyquist frequency method and checkerboard tests. We evaluate and validate the geodetic strain rate results from both a statistical (i.e., based on the Bayesian factor) and quantitative (i.e., based on the comparison with the 2-D analytical strain rate result) approaches. Third, we use our new geodetic strain rate model to estimate seismicity rates.

## 1. Introduction

China is known to have widespread tectonic activity and significant seismic hazards. Profound interactions between the Eurasian, Pacific, and Indian plates have resulted in mountain belts, neotectonic activity, and a high frequency of interplate and intraplate earthquakes (i.e., Zhang et al., 1984). Assessing earthquake hazards in China is particularly challenging not only because of interfering influences among complex fault systems but also due to distributed seismicity within mainland China (i.e., Liu et al., 2007; Wang et al., 2011; Zhang et al., 2013).

In an effort to better understand the distribution of deformation and seismic hazards of this region, Global Positioning System (GPS) measurements have been collected in the past three decades, which have greatly refined our knowledge of crustal kinematics and allowed for studies of lithospheric dynamics (i.e., Fielding et al., 2013; Gan et al., 2007; Ge et al., 2015; Huang et al., 2014; Liang et al., 2013; Rui & Stamps, 2016; Shen et al., 2009; Tong et al., 2010; Wang et al., 2001, 2003, 2008, 2011; Zhang et al., 2004). Two major outcomes of GPS networks, the instantaneous strain rate and variations of the interplate coupling, have played an important role in assessing the seismic hazard of active tectonic areas around the world (e.g., Kreemer et al., 2014; Loveless & Meade, 2010; McCaffrey et al., 2007; Métois et al., 2012; Riguzzi et al., 2012; Wang et al., 2011). The hypotheses of the interplate coupling method assume the entire lithosphere to be plate-like in behavior where the interseismic velocity field can be explained by a combination of rigid block rotation and fault locking within interseismic period; however, many studies consider the behavior of deforming continental lithosphere continuous (Flesch et al., 2001; Liu et al., 2007; Molnar, 1988; Molnar & Tapponnier, 1975; Zhang et al., 2013). In this study, we calculate a continuous strain rate model derived from the GPS velocity gradient, with no assumption of fault or plate features, and use it as the first-order indicator of the regional seismic risk.

In the past decades, numerous of strain rate calculations have been carried out in and surrounding mainland China. Several of the studies focus on areas locally (i.e., Allmendinger et al., 2007; Ge et al., 2015; Wang & Wright, 2012; Zhang et al., 2004, 2018) and others more broadly (i.e., Kreemer et al., 2014; Zheng et al., 2017; Zhu & Shi, 2011). To depict the strain rate pattern of the whole area of mainland China, Zhu and Shi (2011) utilize sparse GPS data only from 1999 to 2005. Kreemer et al. (2014) incorporate most of the published velocities of China during 1999–2013 into the Global Strain Rate Model v2.1. Zheng et al. (2017)

combined the GPS data spanning 1999–2015 in mainland China with velocity solutions of Kreemer et al. (2014) to derive an augmented velocity field of the region.

In this study, to obtain a robust tectonic velocity solution in mainland China, instead of aligning the published velocity sources together following Kreemer et al. (2014) and Zheng et al. (2017), we process ~2,700 GPS data spanning 1996 to 2017 provided by the Crustal Movement Observation Network of China (hereafter called CMONOC) and the Nevada Geodetic Laboratory combined with 10 other velocity solutions outside of mainland China (see section 4. for data doi references) to produce a tectonic velocity solution of this region. We impose an editing scheme on the raw GPS time series to account for postseismic signals associated with the 6 Mw $\geq$ 7 earthquakes that took place inside of the study area during the data collection period and 2 Mw $\geq$ 9 earthquakes outside the study region. We then produce a new geodetic strain rate model for China under the optimal mesh grid definition determined by a novel checkerboard test. Finally, we quantitatively evaluate and validate the tectonic velocity solution and strain rate solution and calculate a tectonic forecast of shallow seismicity of our study area.

## 2. Tectonic Setting of Mainland China

Figure 1 shows a simplified tectonic map of China following the descriptions by Deng et al. (2007), Shen et al. (2009), Li, Li, et al. (2012), Zhang et al. (2013), Yang et al. (2014), and Xu et al. (2017). An assembly of cratonic blocks along orogenic belts, approximately follow the 105°E longitude (i.e., Liu et al., 2007; Wang et al., 2011), is traditionally used to divide China into eastern and western domains (i.e., Wang et al., 2011; Zhang et al., 2013; Zheng et al., 2013).

Eastern China is primarily composed of the North China Block, the South China Block, the Southeastern Asia block, and oil- and gas-bearing basins (i.e., Bohai Bay and South Sea; Gilder et al., 1999; Qi et al., 2008; Zhang et al., 2013). The North China Block (enclosed by brown dotted outline in Figure 1), with its concentrated high tectonic activities, can be further divided into the Ordos block, the North China Plain, and the coastal regions subdivided by the Qinling-Dabieshan fault belt, the Tancheng-Lujiang (Tan-Lu) fault belt, the Zhangjiakou-Bohai fault belt, and the Shanxi Graben (i.e., Liu et al., 2007; Wang et al., 2011; Zhang et al., 2013). Collision between the North and South China Blocks and the convergence between the Eurasian, Pacific, and Philippian plates dominates the present-day crustal deformation, topographic variations, and seismic activities in eastern China (Liu et al., 2007; Wang et al., 2011; Zhang et al., 2013; Zheng et al., 2013). However, due to cratonic regimes of the South China Block and the Southeastern Asia block and the impact of the Pacific and Philippian plates being diminished because of two natural barriers, the Japan and Taiwan island arcs (Zhang et al., 2013), the rate of Quaternary crustal deformation in eastern China is much lower than in western China (Liu et al., 2007).

Western China is primarily composed of the Tibetan Plateau, major orogenic belts (i.e., the Himalaya, Karakorum-Jiali, Kunlun, Altyn Tagh, Qilian and Tianshan orogenic belts), and oil- and gas-bearing basins (i.e., the Tarim, Qaidam, and Junggar basins; i.e., Zheng et al., 2013). The Tibetan Plateau, which formed from the Indian-Eurasian continental collision since 60–50 million years ago, is the most prominent tectonic feature in this region. The present-day Tibetan Plateau is surrounded by the highest peaks globally in the Himalayas, the Karakoram, and Pamir mountain ranges, allocating tremendous gravitational potential energy gradients that dominate the deformation pattern of large parts of central and eastern Asia (e.g., Flesch et al., 2001; Molnar & Tapponnier, 1975). Whereas the Tibetan plateau has formed mainly by N-S shortening during the Indian-Eurasian collision, observations from Quaternary and active faulting, Landsat imagery, fault plane solutions of earthquakes, and geodetic deformation all indicate that for the past ~10 Myr, the tectonic regime has experienced a widespread and marked component of extension within the plateau (e.g., Armijo et al., 1986; Chen et al., 2004; Ge et al., 2015; Liu et al., 2007; Yin et al., 1999). How the Tibetan Plateau deforms is still subject to debate. One school of thinking regard the entire lithosphere to be plate-like in behavior (e.g., Avouac & Tapponnier, 1993; Tapponnier et al., 2001) and the other school considers the behavior of deforming continental lithosphere as continuous (e.g., England & Houseman, 1986; Flesch et al., 2001; Royden et al., 1997).

Beyond the spatial extent of the Tibetan Plateau, there are several other salient tectonic features in the western region; for example, the Altyn Tagh fault is the largest strike-slip fault in central Asia (e.g., Li, Li, et al., 2012), the Tian Shan orogen is one of the most spectacular and active intracontinental young mountain belts

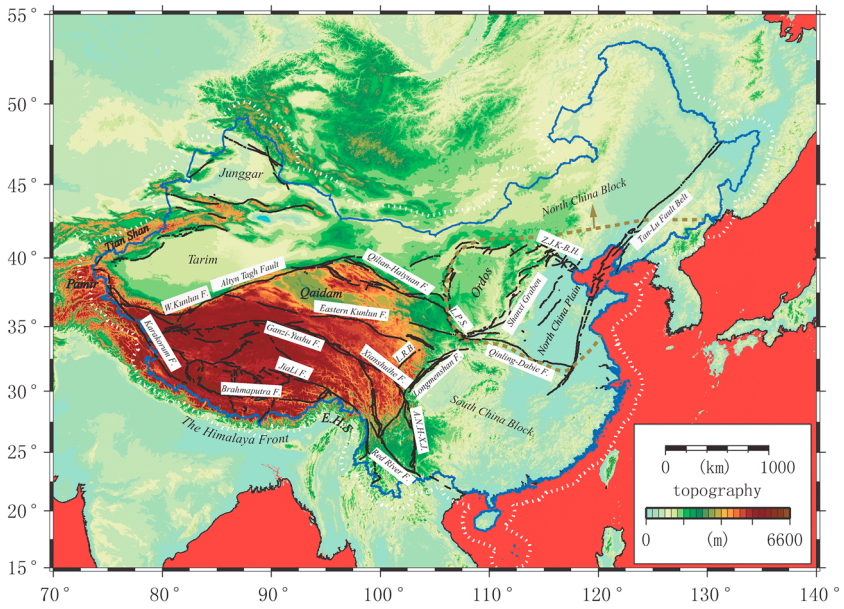


**Figure 1.** Simplified map of the major tectonic units used in this study. The dark brown regions highlight the Tibetan Plateau and its surroundings. The blue outline denotes the political boundaries of China. White dotted outline denotes the 2° (~200 km) outward of China incorporated in this study. The black lines represent faults based mainly on Deng et al. (2007), Shen et al. (2009), Zhang et al. (2013), Li, Li, et al. (2012), and Xu et al. (2017). The brown dotted outline highlights the North China Block. F. = fault; W. Kunlun F. = Western Kunlun Fault; L.R.B = Longriba Fault; A.N.H-X.J = Anninghe-Xiaojiang Fault Zone; E.H.S = the eastern Himalayan Syntaxis; L.P.S = Liupanshan fault; Z.J.K-B.H = Zhangjiakou-Bohai fault zone.

in the world (e.g., Yin & Harrison, 2000), and the Xianshuihe fault is one of the world's most active faults, having produced at least eight earthquakes with magnitude ≥M7 along a 350-km length of the fault since 1725 (e.g., Allen et al., 1991).

The seismic activity in western China is more intense than that in eastern China, in both frequency and magnitude, for example, through recorded history, more than 90 earthquakes with ≥M7 have occurred in western China and less than 30 in eastern China (i.e., Zhang et al., 2013). With the exceptions of the cratonic Tarim basin, the Junggar basin, and the Ala Shan Desert, the seismicity in western China is widely distributed around the Tibetan Plateau, the Tianshan orogenic belt, and Chuan-Dian region.

## 3. Tectonic GPS Velocity Solution

The main focus of our work is on the region of the Chinese Mainland; however, to depict a clearer kinematic picture of this area, we chose to expand our research zone ~200 km outward (white dotted outline in Figure 1). This expansion of the region allows for modeling of some salient tectonic features closely connected to mainland China, such as the Himalaya Frontal Thrust fault system, the eastern Himalayan Syntaxis, the Tian Shan orogenic belt, and the Pamir plateau.

The GPS data we process are mainly from three sources: (1) the Crustal Movement Observation Network of China (CMONOC), operated by the China Earthquake Administration. This network contains ~2216 campaign GPS sites and 400 continuous GPS sites. Some of the CMONOC observation epochs date back as early as 10 March 1999. We process the data up to as late as 28 July 2017. (2) The time series provided by the Nevada Geodetic Laboratory, in which 58 continuous GPS sites are located along Nepal-Bhutan-China boundary and 25 continuous sites along Tajikistan-Kyrgyzstan-China boundary (see section 4 for data references). The observation epochs of these sites span 1 January 1996 to 15 July 2017. We note that the 25 aforementioned sites are only used for translating velocity solutions into a consistent reference frame and are not used to constrain the strain rate calculation. Therefore, we do not include them in our data references. (3) Ten other previously published velocity solutions, sites of which are mainly located within the

prementioned 200-km outward expansion region (Banerjee et al., 2008; Devachandra et al., 2014; Gahalaut et al., 2013; He et al., 2013; Ischuk et al., 2013; Jouanne et al., 2014; Mohadjer et al., 2010; Schiffman et al., 2013; Vernant et al., 2014; Zubovich et al., 2010).

During the collection period of GPS data, there were at least 6 Mw $\geq$ 7 earthquakes that occurred inside of our study area (the 1999 Mw 7.6 Chi-Chi, the 2001 Mw7.8 Kunlun [Kokoxili], the 2008 Mw 7.9 Wenchuan, the 2010 Mw 7.0 Yushu, the 2014 Mw 7.0 Yutian, and the 2015 Mw 7.8 Gorkha [Nepal] earthquakes) and 2 Mw $\geq$ 9 earthquakes outside (the 2004 Mw 9.3 Sumatra and the 2011 Mw 9.0 Tohoku-oki earthquakes), which had a significant impact on the interseismic velocity field of the mainland China. In some studies, postseismic transients are modeled by using analytical methods, for example, by fitting and removing the transient signals with logarithmic or/and exponential decay functions (Marone et al., 1991; Nur & Mavko, 1974; Savage, 1990). In this study we remove data that were likely affected by the events following the approaches described below to derive a secular velocity solution independent of coseismic and postseismic effects.

We process all of the 2,700 GPS sites from sources 1 and 2 using the following seven step approach: (1) For each of the eight earthquakes, if it occurred after 2008 (the 2011 Mw 9.0 Tohoku-oki, the 2014 Mw 7.0 Yutian, and the 2015 Mw 7.8 Gorkha [Nepal] earthquake), we will only utilize data before the earthquake to calculate the velocity solution for sites affected by this earthquake (the affected area is estimated following equation (1) below). For earthquakes that occurred before 2008 (the 1999 Chi-Chi earthquake, the 2011 Kunlun earthquake, and 2004 Sumatra earthquake), we only utilize data 5 years after the earthquake to calculate the velocity solution. (2) If using preseismic data to estimate the velocity solution, for campaign sites, we require them to have at least 4 years length of data, 4 epochs of observation, and weighted root-mean-square (WRMS) statistics of time series being less than 2.0 mm. Otherwise, the site is discarded. For continuous sites, at least 2.5-year length of data and the same WRMS criteria are required. A 2.5-year interval is selected according to Blewitt and Lavallée (2002), which demonstrate that GPS data can be characterized with a minimum bias in the velocity solution for data sets with the 2.5-year limit plus 0.5-year time intervals by modeling sinusoid signals. (3) If using the postseismic data to estimate the velocity solution, at least 6 years of observation length for campaign sites and 3.5 years for continuous sites are required. The other postseismic data editing criteria are the same as that described in (2). We restrict the editing standard for postseismic data mainly to ascertain that the relatively stable equilibrium state is established for the earthquake affected area following studies of Meade and Loveless (2017). (4) Because of the sparsity of sites surrounding the epicenters of 2015 Nepal earthquake and 2014 Yutian earthquake, we loosen the observation length limit on campaign sites from 4 to 3 years but restrict the WRMS statistics from being less than 2.0 mm to being less than 1.5 mm. With such an adjustment of the editing scheme, 26 more sites are included (nine sites in the Yutian earthquake affected area and 17 in the Nepal earthquake). (5) The radius of influence of an earthquake is approximated using the empirical formula (Herring, Melbourne, et al., 2016),

$$d = 2.5\times10^{-3}\times5^{M} \tag{1}$$

where $M$ is the magnitude of the earthquake as reported by the U.S. Geological Survey National Earthquake Information Center. All stations within $d$ km of the epicenter are then edited with the aforementioned processing strategies and rechecked visually. (6) To account for the tremendous impact of the postseismic relaxation of 2011 Mw 9.0 Tohoku-oki earthquake (i.e., Zhao et al., 2015), we decide to remove all the data collected after this earthquake for sites with longitude greater than 110°E (Figure 1). (7) For the earthquakes with lower magnitude, 5.8 $\leq$ Mw $\leq$ 7.0, we evaluate the time series of their affected GPS sites. If no obvious postseismic signals are found, we simply apply a heaviside step function to correct for coseismic offsets. Otherwise (e.g., sites affected by 2014 Mw 6.0 Kangding earthquake), we will follow the same procedures described above to issue the data editing.

For the CMONOC data, we process the raw GPS data loosely following the procedures described in McClusky et al. (2000), McCaffrey et al. (2007), and Rui and Stamps (2016) using the GAMIT-GLOBK GPS processing software (Herring, King, et al., 2016). We combine the phase observations from the GPS receivers with observations from 5 to 10 continuous International GNSS Service (IGS) stations to estimate loosely constrained positions, atmospheric parameters, and Earth orientation parameters, each with associated covariance matrices. We then combine these estimates and their covariances as *quasi-observations*

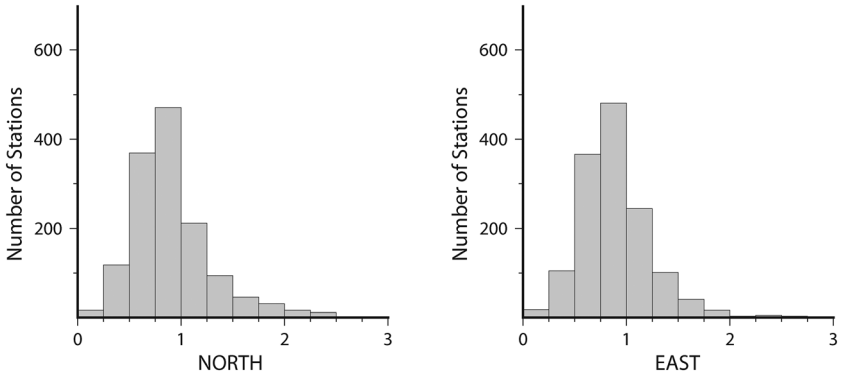


**Figure 2.** Global Positioning System (GPS) normalized root-mean-square histogram of position estimates.

(Dong et al., 1998) with the estimates and covariances from the MIT global analysis to estimate daily positions. Then, for continuous sites, we aggregate the daily estimates over periods of 7 days to better assess the long-term statistics of the positions following McCaffrey et al. (2007). For the campaign sites, we directly use the daily estimate. We combine the position estimates into a cumulative solution to derive site velocities for the episodic and continuous sites separately, and then rotate and translate the two solutions into the Eurasian fixed 2008 International Terrestrial Reference Frame (ITRF2008; Altamimi et al., 2012) with 58 common IGS sites distributed around the world.

Realistic uncertainties for the estimated position coordinates and velocities are obtained by adding both white and correlated noise to the phase observations and daily quasi-observations. To do so, we first assign 10 mm for the a priori phase observations error to make coordinate uncertainties approximately realistic with 2-min sampling following Herring, King, et al. (2016). We then remove apparent outliers and down-weight the daily observations for stations and time periods that reflect a higher than average scatter. Next, we add a random-walk component to all continuous stations that we determined using the first-order Gauss-Markov (FOGMEX) algorithm (Herring, 2003; Reilinger et al., 2006). Lastly, an estimate for random-walk noise is added to the campaign data based on the average of its three closest continuous stations. After adding the correlated noise, we recalculate the uncertainties of the velocity solutions.

To assess whether our noise model describes the error characteristics during phase processing stage, following McCaffrey et al. (2007), we evaluate the normalized rms (NRMS) of all of time series. As shown in Figure 2, the NRMS histogram is approximately normal with a mean value of ~0.8 in both components. As stated in McCaffrey et al. (2007), a value less than 1.0 is a reasonable target since we expect the scatter in the time series to underestimate the true uncertainties in the velocity estimates, which should contribute significantly from correlated noise (we added this only in the velocity solution). We also calculate the average velocity uncertainties for the north and east components after adding the correlated noise, which are ~0.28 and ~0.26 mm/year, respectively. The relatively lower uncertainties compared to several published velocity solutions in this region (Kreemer et al., 2014; Li, You, et al., 2012; Liang et al., 2013), even using the same data set, is due to our data editing criteria described above.

We use the position time series provided by the Nevada Geodetic Laboratory to derive their corresponding velocity solutions (see section 4), of which we add the random-walk component to all the stations based on the FOGMEX algorithm.

There are 10 published velocity solutions located within the ~200 km outward *expansion* region (Table 1; Banerjee et al., 2008; Devachandra et al., 2014; Gahalaut et al., 2013; He et al., 2013; Ischuk et al., 2013; Jouanne et al., 2014; Mohadjer et al., 2010; Schiffman et al., 2013; Vernant et al., 2014; Zubovich et al., 2010), of which we could not access their raw GPS data. To utilize these existing velocities to augment our solution, we transform each velocity solution into Eurasian fixed-reference frame using Euler poles determined by Altamimi et al. (2012). We find and compare the velocity solutions of common IGS sites between the transformed velocity solution and our new velocity solution. If there are more than three common IGS sites, and the residual velocities are randomly directed and with the average magnitude less than ~1.5 mm/year, we incorporate the velocities into our new solution. If the velocity residuals are not random, rather they

**Table 1**
*Overview of the 10 Published Velocity Sources and Alignment Statistics to Our New Tectonic Velocity Solution*

| Published sources | Study area | Velocity frame | Mean_Vdiff (mm/yr) | Max_Vdiff (mm/yr) | Common sites |
|---|---|---|---|---|---|
| Banerjee et al. (2008) | The Indian subcontinent | ITRF00 | 1.19 | 1.61 | 15 (MUNN, CSOS, GHTY, GHTU, IISC, HYDE, LUMA, TZPR, LHAS, IRKT, KSTU, URUM, POTS, SEY1, DGAR) |
| Devachandra et al. (2014) | the eastern Himalayan Syntaxis | ITRF08_EURA | 1.18 | 2.08 | 5 (URUM, HYDE, IISC, POL2, KIT3) |
| Gahalaut et al. (2013)[a] | the Indo-Burmese wedge | ITRF05 | 0.96 | 1.52 | 4 (LUMA, TZPR, GHTU, GHTY) |
| He et al. (2013) | the Altyn Tagh fault | ITRF08 | 1.41 | 1.86 | 4 (HYDE, IRKT, POL2, URUM) |
| Ischuk et al. (2013) | the Pamir-Hindu Kush | ITRF08_EURA | 0.67 | 1.14 | 5 (BJFS, HYDE, IRKT, LHAZ, WUHN) |
| Jouanne et al. (2014)[a] | The northern Pakistan | ITRF08 | 1.05 | 1.75 | 6 (1902, 1903, 2203, 2205, PK24, PK28) |
| Mohadjer et al. (2010) | the Pamir-Hindu Kush | ITRF05_EURA | 1.46 | 1.91 | 4 (HYDE, IISC, POL2, KIT3) |
| Schiffman et al. (2013)[a] | the Kashmir Himalaya | ITRF05_INDI | 0.86 | 1.79 | 7 (RANK, MULG, CONV, NISH, NARA, SON1, KARG) |
| Vernant et al. (2014) | the eastern Himalayan Syntaxis | ITRF08_INDI | 0.54 | 1.22 | 7 (BJFS, HYDE, KIT3, KUNM, POL2, URUM, XIAN) |
| Zubovich et al. (2010) | the Tien Shan | ITRF05_EURA | 0.37 | 0.66 | 7 (CHUM, KAZA, PODG, POL2, SELE, SUMK, TALA) |

*Note*. Common sites give the Institute of Geological Sciences sites used for velocity alignment. Mean_Vdiff and Max_Vdiff denote the average and maximum velocity differences between the two velocity solutions after alignment.
[a]Means using the sites separated by up to, for example, 50 km to align the frames for lack of co-located Institute of Geological Sciences sites. EURA and INDI represent the Eurasian and India fixed-reference frameworks, respectively.

are systematically directed, we will assume that the discrepancies are due to reference frame difference and employ a seven-parameter transformation (three translations, three rotations, and one scale) to align the two velocity fields into a common reference frame by minimizing the residual velocities (Loveless & Meade, 2010). If less than three common IGS sites exit between the two solutions, we utilize the sites separated by less than ~50 km to align the frames.

Banerjee et al. (2008) provide the observation duration information for each of their sites; we remove the sites with observation time shorter than 2 years or observation epochs less than 4. Ischuk et al. (2013) provide

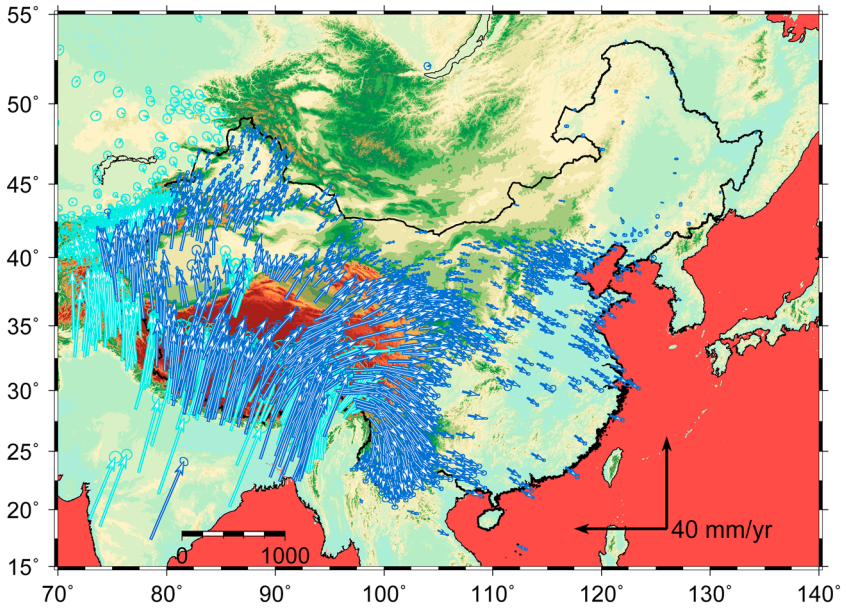


**Figure 3.** The tectonic Global Positioning System (GPS) velocity field derived from continuous and episodic GPS data of Crustal Movement Observation Network of China (CMONOC) network and the Nevada Geodetic Laboratory spanning 1996–2017 (blue open arrows) and incorporation of 10 previously published sources (light green open arrows). The velocity vectors are plotted with 2-sigma uncertainty (95% confidence ellipse).

**Table 2**
*Stations Used From the Nevada Geodetic Laboratory That Have DOI References*

| Lon | Lat | Site name | Doi |
|---|---|---|---|
| 80.50093 | 29.73381 | DRCL_NGL | doi:10.7283/T50863FX |
| 80.58178 | 28.75444 | DNGD_NGL | doi:10.7283/T53X84S2 |
| 80.62619 | 29.17652 | GNTW_NGL | doi:10.7283/T5CF9N74 |
| 81.20069 | 29.47417 | BYNA_NGL | doi:10.7283/T59G5JZH |
| 81.5953 | 28.11717 | NPGJ_NGL | doi:10.7283/T5M043JB |
| 81.61535 | 28.04935 | NEPJ_NGL | doi:10.7283/T5XW4H4P |
| 81.71436 | 28.65582 | BMCL_NGL | doi:10.7283/T5H70CZ0 |
| 81.80654 | 29.96939 | SMKT_NGL | doi:10.7283/T55T3HM2 |
| 81.82111 | 29.96837 | SKOT_NGL | doi:10.7283/T5PG1Q2T |
| 82.19257 | 29.27782 | JMLA_NGL | doi:10.7283/T57P8WHD |
| 82.4912 | 27.95081 | GRHI_NGL | doi:10.7283/T5VH5M03 |
| 82.81789 | 28.98368 | DLPA_NGL | doi:10.7283/T5QR4V8C |
| 82.98671 | 28.10126 | PYUT_NGL | doi:10.7283/T54T6GH4 |
| 83.60329 | 27.76685 | KLDN_NGL | doi:10.7283/T56Q1VCK |
| 83.7433 | 28.80528 | JMSM_NGL | doi:10.7283/T5Z899K1 |
| 83.76346 | 28.34509 | DNSG_NGL | doi:10.7283/T5D798K9 |
| 83.82572 | 27.45736 | BELT_NGL | doi:10.7283/T52J68Z3 |
| | | BELT_NGL | doi:10.7283/T56971NC |
| 83.93581 | 28.26021 | SRNK_NGL | doi:10.7283/T5K072DZ |
| 84.38535 | 27.66824 | CHWN_NGL | doi:10.7283/T5J1019K |
| 84.57341 | 28.17412 | LMJG_NGL | doi:10.7283/T58K776D |
| 85.10768 | 27.60814 | DAMA_NGL | doi:10.7283/T5SX6BK9 |
| 85.31408 | 28.20723 | CHLM_NGL | doi:10.7283/T5TH8JV9 |
| 85.79886 | 27.38483 | SNDL_NGL | doi:10.7283/T5125QSQ |
| 86.55001 | 27.30513 | RMJT_NGL | doi:10.7283/T5SJ1HQG |
| 86.59706 | 26.99095 | RMTE_NGL | doi:10.7283/T5X928F6 |
| 86.71246 | 27.81423 | SYBC_NGL | doi:10.7283/T5222RX3 |
| 87.27219 | 26.51971 | BRN2_NGL | doi:10.7283/T5NS0S05 |
| 87.28125 | 26.43867 | BRNG_NGL | doi:10.7283/T5PR7T40 |
| 87.39214 | 26.86609 | ODRE_NGL | doi:10.7283/T5BG2M39 |
| 87.70982 | 27.35224 | TPLJ_NGL | doi:10.7283/T5G73BTM |

the daily position repeatability of their sites; we remove the sites with observation epochs less than 3. Before incorporating the transformed velocities into our final solution, we remove all the sites with velocity uncertainties larger than 1 mm/year for either the north or east component, but with two exceptions. First, we loosen the criteria to be 1.5 mm/year for the velocities of Banerjee et al. (2008) because of the limited data quality during 2008. Second, we loosen such criteria to be 2 mm/year for the velocities of Vernant et al. (2014). This approach allows inclusion of more sites around the eastern Himalayan Syntaxis. After incorporating each velocity solution there are locations with two sites. For these sites, we retain our solution provided we have processed raw data. Otherwise, we average the velocities using their inverse of standard error as weight.

Our final tectonic velocity solution consists of 1,755 sites and is shown in Figure 3. About 1,079 of which are from CMONOC network, 54 are from Nevada Geodetic Laboratory and 622 are from the 10 published sources. The full velocity solution is provided in Data Set S1 in GLOBK velocity format.

## 4. Data References

Here we provide available citation information for GPS data obtained from the Nevada Geodetic Laboratory in Table 2 document in order to abide by the FORCE11 data citation principles (Martone, 2014) and FAIR (Findable, Accessible, Interoperable, Reusable) data principles (Wilkinson et al., 2016).

## 5. Geodetic Strain Rate

### 5.1. Mesh Definition

Several previous studies define the size of their model meshes to be comparable to the average distance of geodetic sites (i.e., Hackl et al., 2009; Zeng et al., 2018), which is appropriate when the sites are evenly distributed. However, in this study, the GPS sites are densely distributed along the major active faults, plate boundaries, and some economically developed cities but sparsely deployed in other regions. Thus, to find a proper mesh dimension for strain rate modeling of this region, we determine it based on the Nyquist frequency method and a checkerboard test approach.

First, following the Nyquist frequency concept, the spatial resolution of observation data with sampled points should be at most half the average spacing between the closest point pairs (Hengl, 2006),

$$p \leq \frac{\overline{h}_{ij}}{2} \tag{2}$$

where $\overline{h}_{ij}$ is the mean shortest distance of point pairs. Based on the geometry of GPS sites in this study, we get the spatial resolution $p$ being no more than 36.4 km or ~0.33°. This result implies that our grid spacing should not be smaller than 0.33°.

Second, we employ a novel form of the checkerboard test to determine the optimal mesh grid definition that is analogous to checkerboard resolution tests of fault slip models (Bügmann et al., 2005; Loveless & Meade, 2010; Métois et al., 2012). To conduct the checkerboard test of a fault slip model, one applies alternating fault slip to a discretized fault geometry arranged in a checkerboard. The test then involves calculating surface velocities at station coordinates that would result from the simulated slip pattern. Finally, an inversion is performed for slip on the fault surface to test the degree to which one can recover the input checkerboard slip pattern (i.e., Loveless & Meade, 2010).

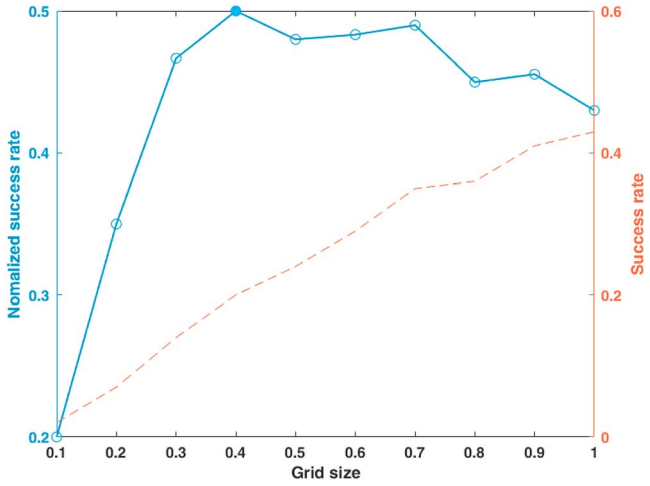


**Figure 4.** The success rate (percentage of ratio falling between 0.5 and 1.5, dashed line) and normalized success rate (the success rate in a normalized area of 1° × 1°, solid line) for patch sizes of 0.1° × 0.1° to 1.0° × 1.0°. Our preferred model, with maximum normalized success rate, is 0.4° × 0.4°.

Instead of applying alternating slip patterns as in the fault slip checkerboard test, we apply an analogous east component of *modeled* velocities. These modeled velocities are applied to patches of a discretized mesh arranged as a checkerboard (Figure S2). Strain rates are then calculated from the *modeled* velocities, which we refer to, hereafter, as modeled strain rates. We sample modeled velocities at GPS station coordinates and calculate *observed* strain rates. Finally, we evaluate the degree to which the observed strain rates can recover the modeled strain rates at different mesh dimensions.

We test meshes that are discretized by 0.1° × 0.1°, 0.2° × 0.2°, 0.3° × 0.3°, 0.4° × 0.4°, 0.5° × 0.5°, 0.6° × 0.6°, 0.7° × 0.7°, 0.8° × 0.8°, 0.9° × 0.9°, and 1.0° × 1.0° size patches. We calculate a ratio of the observed to modeled second invariant of strain rates to evaluate to what extent the observed strain rate can match the modeled strain rate. Figure S3 shows examples of the ratio distributions. Figure 4 shows the percentage of the ratio that falls between 0.5 and 1.5 (hereafter called success rate) for patch sizes of 0.1° × 0.1° to 1.0° × 1.0°. We see a continuous increase of success rate with patch size increased (dashed orange line). However, the larger the patch size, the worse the spatial resolution of strain rate. Therefore, to find a trade-off between patch size and success rate, we normalize the success rate by dividing the corresponding grid size. The result is shown in Figure 4 (thick solid line), from which 0.4° × 0.4° gives the highest percentage of normalized success rate.

Based on the Nyquist frequency and checkerboard tests, we choose 0.4° × 0.4° as the optimal dimension of mesh grid to conduct the strain rate model.

### 5.2. Methodology

We adopt the methodology described by Haines and Holt (e.g., Beavan & Haines, 2001; Haines et al., 1998; Haines & Holt, 1993) to invert our velocity solution to derive a new present-day tectonic strain rate field throughout mainland China and its surroundings in spherical coordinates. A bi-cubic Bessel interpolation (Beavan & Haines, 2001; Kreemer et al., 2014) is used to obtain a continuous velocity gradient tensor field by a least squares minimization between modeled and observed velocities, with the trade-off of minimizing the strain rates subject to their respective a priori variance parameter (Appendix A.5 of Beavan and Haines, 2001). We assign no a priori rigid zones in the model to allow our tectonic GPS velocity solution to constrain the strain rate field as a continuum.

To assign a priori strain rate (co)variances to each deforming grid cell, we follow the two-step approach described in Kreemer et al. ( 2014). In the first step, we assign a uniform standard deviation of $2 \times 10^{-8}$ for $\dot{\varepsilon}_{\varphi\varphi}$, $\dot{\varepsilon}_{\theta\theta}$, and $\dot{\varepsilon}_{\varphi\theta}$ to all cells, with zero covariances. In the second step, we take the modeled strain rate field from the first step to constrain a priori standard deviations. That is, we defined a priori standard deviation of $\dot{\varepsilon}_{\varphi\varphi}$, $\dot{\varepsilon}_{\theta\theta}$ to be same as the second invariant ($\sqrt{\dot{\varepsilon}^2_{\varphi\varphi} + \dot{\varepsilon}^2_{\theta\theta} + 2\dot{\varepsilon}^2_{\varphi\theta}}$) of the tensor modeled in step 1 and standard deviation of $\dot{\varepsilon}_{\varphi\theta}$ to be $\sqrt{\left(\dot{\varepsilon}^2_{\varphi\varphi} + \dot{\varepsilon}^2_{\theta\theta} + 2\dot{\varepsilon}^2_{\varphi\theta}\right)/2}$.

### 5.3. Results

Figure 5 shows the second invariant, or magnitude, of the final strain rate field. The most striking feature is the difference of the strain rate magnitudes accommodated by western and eastern China. The regions with the highest magnitude strain rates are mainly located in western China along the Himalayan arc (~0.06–0.09 $10^{-6}$/year), the eastern Himalayan Syntaxis (~0.03–0.11 $10^{-6}$/year), the Pamir plateau (~0.09–0.10 $10^{-6}$/year), and the Xianshuihe-Xiaojiang fault belt (~0.05–0.09 $10^{-6}$/year). Apart from these locations, the second invariants along the Altyn Tagh fault belt, the Haiyuan fault, the Longriba fault, and westernmost of the Qiangtang block are accommodating relatively low-magnitude strain rates (~0.03–0.04 $10^{-6}$/year), but they are distinguishable from their surroundings. In eastern China, the second invariants are mainly distributed along the boundaries of the Ordos block (~0.02–0.03 $10^{-6}$/year), the interior of the North China Plain (~0.02

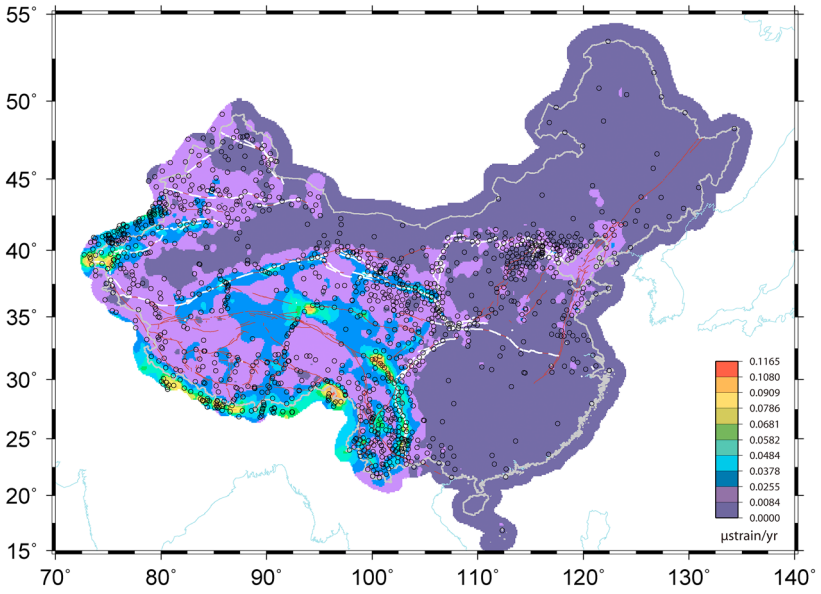


**Figure 5.** The second invariant of the tectonic strain rate model. The white dotted lines highlight approximately the outlines of the Tibetan Plateau, the North China Block, and the Tian Shan orogenic belt. The circles indicate the locations of Global Positioning System (GPS) stations.

$10^{-6}$/year), the Zhangjiakou-Bohai fault belt (~0.02 $10^{-6}$/year), and the Tan-Lu fault belt (~0.02 $10^{-6}$/year), which are consistent with the relatively intense distribution of seismic activities in this region.

The dilatational component of the strain rate tensor is shown in Figure 6, in which the positive values indicate the extension and negative values indicate the compression. The principal long-wavelength features in the areal strain rate are: (1) pronounced extension within the Tibetan Plateau and contraction on its margins; (2) the Tian Shan belt shares comparable amounts of contraction rate with that of the Himalaya arc. The contraction in eastern Tian Shan is more dispersed than in western Tian Shan, which was also observed

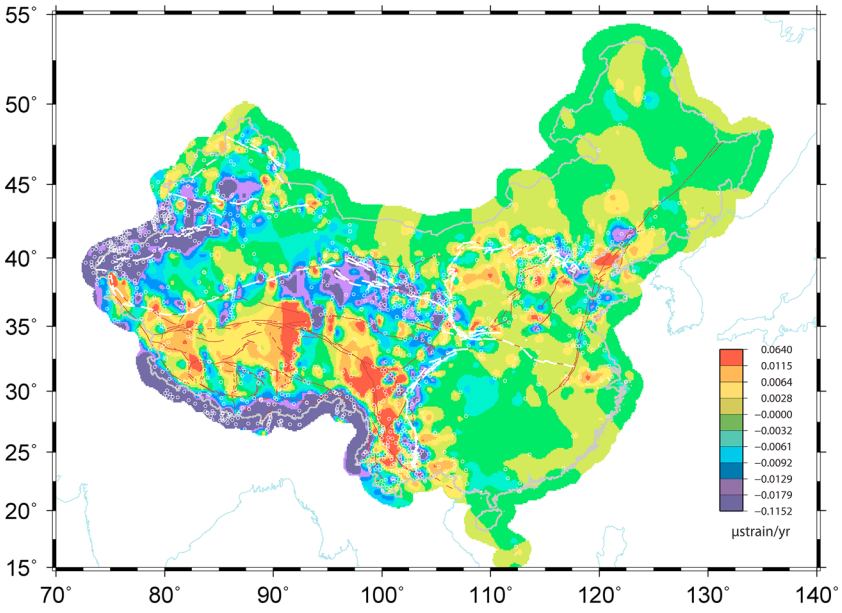


**Figure 6.** Dilatational strain rate. The positive values indicate the extension and the negative values indicate the compression.

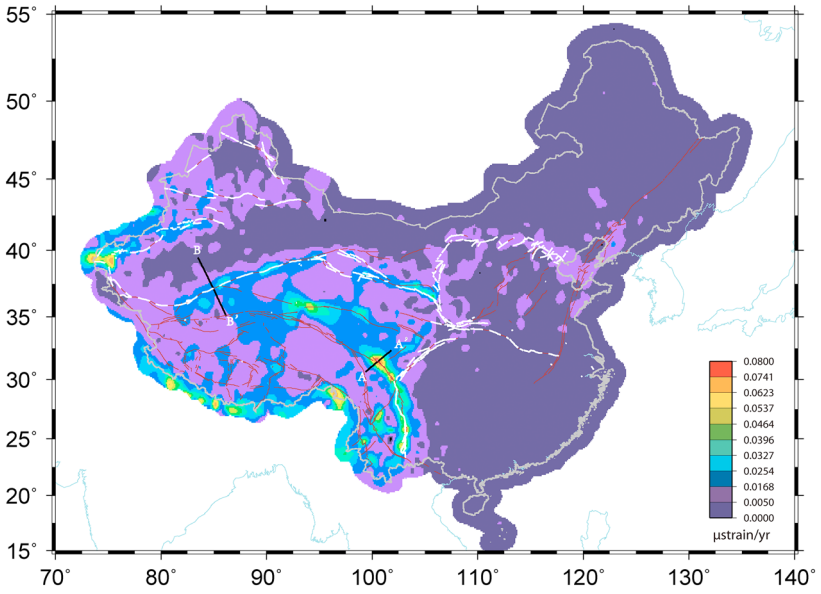


**Figure 7.** The maximum shear strain rate. AA′ and BB′ denote profiles across the Xianshuihe and Altyn Tagh faults that are used for shear strain sampling and strain rate result evaluation. For more details, please refer to section 6.2.

by Li et al. (2015); (3) no apparent areal strain rate in Eastern China except within the North China Block (Figure 1). In particular, gradual change from contraction to extension along the coastline of the Bohai sea (around ~120°E, 40°N) is consistent with the fault plane solutions of historical earthquakes occurred here (i.e., Liu et al., 2007; Zhang et al., 2013). However, because of the very weak velocity gradient signals in this region, a better resolution of the strain rate tensor here requires denser and longer data collection.

Figure 7 shows the maximum shear strain rate result. Broadly, this result shares the similar pattern as that of the second invariant of the strain rate tensor (Figure 5). Eastern China accommodates low-magnitude shear strain rates and western China shears dramatically. The most significant shear strain rates are accommodated along the Xianshuihe-Xiaojiang, the eastern Kunlun, the Altyn Tagh, and the Haiyuan fault zones. The orientations of shear strain signal in these areas rotate and maintain the left-lateral strike slip movement of the corresponding fault zones, which is consistent with their large, long-term geological structures. Concentrated shear strain rates are also found along the Himalayan region, the eastern Tian Shan, and the eastern Himalayan Syntaxis.

## 6. Evaluation of the Strain Rate Results

### 6.1. Statistical Evaluation of the Results

We evaluate our strain rate results using three statistical approaches. First, according to the Bayesian theory, we evaluate the ratio between the posterior and a priori standard deviation of the second invariant. If the a priori variance parameter is properly assigned, the ratio between the posterior and a priori standard deviations (hereafter called the Bayesian factor) should be equal to unity. The Bayesian factor result is shown in Figure S4. For clarity, we only saturate the areas where the Bayesian factor falls between 0.7 and 1.3; the lower and higher extremes are shaded with black and white colors, respectively. Our result shows that for majority of the study area, the Bayesian factors are within the 0.7–1.3 range. The relatively lower Bayesian factors (<0.7) are mainly distributed in the regions with higher GPS site density, while the relatively higher Bayesian factors (>1.2) are located along the boundaries where the GPS site distributions are relatively sparse. These results imply that station spacing has a direct influence on the posterior standard deviation of the strain rate solution; that is, the denser site distribution in a mesh grid will results in the smaller standard deviations of calculated strain rate, which is simply a result of the weighted least square (e.g., Beavan & Haines, 2001; Kreemer et al., 2014).

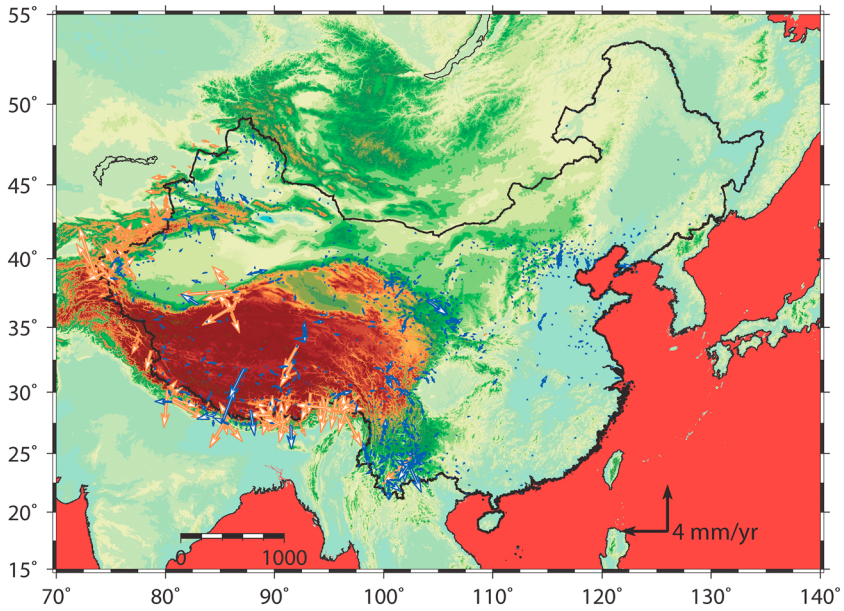


**Figure 8.** Velocity residuals of the best fit strain rate model. The blue and orange arrows represent the sites processed by this study and the published sources, respectively.

In our second approach, we use the normalized RMS of the velocity residuals, which is the unitless indicator of how well the data fit the model:

$$\mathrm{NRMS} = \left(N^{-1}\left(\sum_{i=1}^{N} r_i^2/\sigma_i^2\right)\right) \tag{3}$$

where $r$ is the velocity residual, $\sigma$ is the standard deviation, and $N$ is the number of observations. For this study, $N = 2 \times N_v$, where $N_v$ is the number of velocity data.

Our final strain rate model has an NRMS of 1.06. The magnitudes of velocity residuals are shown in Figure 8. The largest velocity residuals are mostly localized along the westernmost boundary of our study area. Two reasons may cause this result: the current mesh grid definition (0.4° × 0.4°) may be too conservative to capture the rapid and dramatic velocity gradient change in this region and the data quality or framework definition of the previously published velocities is not as consistent as the one derived by this study. The residuals are significantly smaller in this region compared to their interseismic velocities. Therefore, we suggest that the strain rate solution is a trustworthy indicator of the first-order deformation pattern in this region.

Finally, we evaluate the confidence level of strain rate result by computing the signal-to-noise ratio of the second invariant (Figure 9):

$$\left(\sqrt{\dot{\varepsilon}_{\varphi\varphi}^2 + \dot{\varepsilon}_{\theta\theta}^2 + 2\dot{\varepsilon}_{\varphi\theta}^2}\right) \Big/ \sqrt{\mathrm{var}\left(\dot{\varepsilon}_{\varphi\varphi}^2\right) + \mathrm{var}\left(\dot{\varepsilon}_{\theta\theta}^2\right) + 2\,\mathrm{var}\left(\dot{\varepsilon}_{\varphi\theta}^2\right)} \tag{4}$$

As indicated by Kreemer et al. (2014), the signal-to-noise ratio (SNR) ratio reflects the joint effect of signal, noise, and spatial density of the geodetic stations; thus, it is not appropriate to overly interpret it as a pure indicator of confidence level of the strain rate result. Also, interpreting the magnitude of the SNR ratio from a relative viewpoint is more meaningful than the absolute viewpoint, because the noise component can be defined in different ways, for example, Beavan and Haines (2001) defines the standard error of the second invariant to be $\sqrt{\frac{1}{3}\left[\mathrm{var}\left(\dot{\varepsilon}_{\varphi\varphi}^2\right) + \mathrm{var}\left(\dot{\varepsilon}_{\theta\theta}^2\right) + 2\,\mathrm{var}\left(\dot{\varepsilon}_{\varphi\theta}^2\right)\right]}$, while Kreemer et al. (2014) and our work define it to be $\sqrt{\mathrm{var}\left(\dot{\varepsilon}_{\varphi\varphi}^2\right) + \mathrm{var}\left(\dot{\varepsilon}_{\theta\theta}^2\right) + 2\,\mathrm{var}\left(\dot{\varepsilon}_{\varphi\theta}^2\right)}$. Nonetheless, Figure 9 can still provide us the following information: First, the SNR ratio in Figure 9 shares the similar pattern as that of second invariant of strain rate

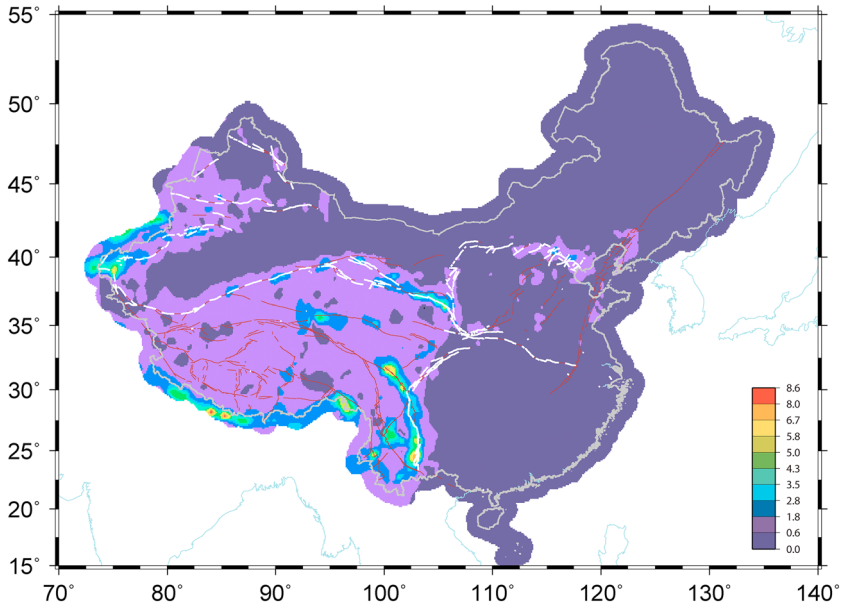


**Figure 9.** Signal-to-noise ratio of the second invariant of the strain rate solution.

tensor shown in Figure 5. This result implies that the uncertainties (noise) of the second invariant signal are at a similar level in the whole study area. Regions with relatively higher SNR values accommodate larger strain rate signals than regions with lower SNR values. Second, in the western China, the Tibetan Plateau and the Tian Shan orogenic belt have relatively higher SNR values. However, we note that in the eastern China, the Zhangjiakou-Bohai and the Tan-Lu fault belt (at about 113–120° longitude and 35–40° latitude; see Figure 1) also have a higher SNR value compared to its surroundings. Considering the high population density and occurrences of great historic earthquakes in that region, we suggest that more attention should be paid to these specific areas (see section 7.2 for further seismic risk discussion). In addition, as noted by Beavan and Haines (2001), the uncertainties of strain rate are also affected by the area of cell; to test such influence, we normalize the strain rate error $E_i^{'} = E_i \times \sqrt{A_i/A_0}$ similar to Beavan and Haines (2001), where $E_i$ is the strain rate error, $A_i$ is the area of cell $i$, and $A_0$ is the average area of all cells in study area. The SNR based on this normalized strain rate error is shown in Figure S5, from which we see little difference compared to Figure 9; regardless, mainland China is located in a midlatitude area such that spherical curvature should have a minimal effect.

### 6.2. Quantitative Evaluation of the Results

As described by Savage and Burford (1973), the 2-D model interseismic velocity profile across a vertical strike-slip fault zone can be given by

$$\mathrm{v}(x) = \frac{V}{\pi}\tan^{-1}\frac{x}{D} \tag{5}$$

where $V$ is the slip rate of the fault, $x$ is the horizontal fault-perpendicular distance, and $D$ is the locking depth. The derivative of the velocity profile across the fault is the shear strain rate (Smith-Konter et al., 2011), given by,

$$\dot{\varepsilon}(x) = \frac{V}{\pi D}\frac{1}{\left(1+\frac{x}{D}\right)^2} \tag{6}$$

Theoretically, for a purely vertical strike-slip fault, the 2-D analytical derived strain rate model should be consistent with that observed by the geodetic data. Therefore, we choose two strike-slip faults, the Xianshuihe fault and the Altyn Tagh fault, as examples to quantitatively evaluate our strain rate solution.

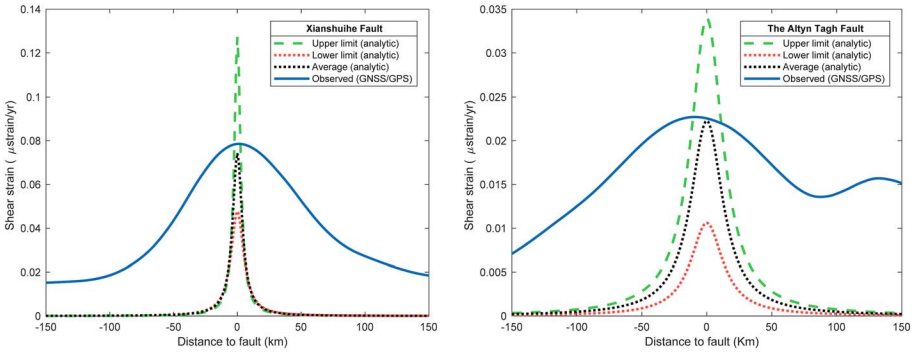


**Figure 10.** Comparison between the observed and 2-D analytic shear strain rate across the Xianshuihe fault (AA′ in Figure 7) and the Altyn Tagh fault BB′ in Figure 7), respectively. The green, red, and black dotted lines represent the upper, lower limits, and medium value of analytic shear strain rate. The blue line denotes the Global Positioning System (GPS)-derived shear strain rate from this study.

To calculate the 2-D analytical model from equation (6), we choose the far-field velocity $V$ (9–12 mm/year) and locking depth $D$ (3–6 km) of the Xianshuihe fault derived from Wang et al. (2009), and $V$ (11 ± 5 mm/year), $D$ (15 km) of the Altyn Tagh fault from Elliott et al. (2008) as the input. The uncertainties of the $V$ and $D$ are utilized to calculate the upper and lower limits of the analytical strain rate. We note that both of these slip rates and locking depths were estimated using interferometric synthetic aperture radar (InSAR) data and are in agreement with the geological results (see Bendick et al., 2000, and He et al., 2013, for detailed discussions on the Altyn Tang fault and Wang et al., 2009, for the Xianshuihe fault).

At the locations in close proximity to where the InSAR satellite tracks are used, for example, AA′ on the Xianshuihe fault and BB′ on the Altyn Tagh Fault (Figure 7), we sample our GPS-derived shear strain rate result and compare them with the aforementioned analytical model. The results are shown in Figure 10, where the blue lines are the GPS-derived strain rate, the green and red dotted lines are upper and lower limits of the analytical strain rate derived from equation (6), and the black dotted lines are the average of the green and red lines. We find the peak values of GPS-observed shear strain rates (blue lines) are in agreement with the averaged analytical strain rate results (black dotted line) derived by equation (6) on both faults (Figure 10). The inconsistency on the two wings of the profiles are mainly due to sparsity of GPS sites and nonoptimal orientation of the stations relative to the fault such that the steep gradient strain rates near the faults cannot be captured. In other words, with current spacing of GPS sites, no matter how to adjust the mesh dimension determined in section 5, the inconsistency between data-derived and model-derived profiles cannot be significantly improved near the location of the fault. As suggested by Smith and Sandwell (2003), to recover the strain rates for faults with a shallow locking depth (≤10 km) requires the spatial resolution of GPS sites to be 2–3 km. A simple dislocation model (e.g., Savage & Burford, 1973) shows that for a strike-slip fault locking at 15 km depth, ~80% of strain accumulation takes place within 30 km of the fault, thus requiring spacing of GPS sites to be at least 15 km to capture the velocity gradient. In addition to the site distribution, the deviation of the profiles may also be affected by unrealistic assumptions that these two faults are completely vertical, purely strike-slip, and complicated by the influence of adjacent faults. Even though there is an inconsistency described above, considering the general agreement among the peak values of geodetic, InSAR, geological, and analytical results, we suggest that with current spacing of GPS points, our GPS-derived strain rate solution can reasonably describe the inter-seismic strain rate of faults and, thus, the interseismic strain accumulation phase of the earthquake cycle.

## 7. Discussion

### 7.1. Comparison With the Global Strain Rate Model v2.1

The Global Strain Rate Model (GSRM) v2.1 published by Kreemer et al. (2014) is now broadly accepted by the community. The model utilizes ~22,511 horizontal geodetic velocities globally to obtain the geodetic strain rates at the resolution of 0.25° longitude by 0.2° latitude. Here we compare our results to GSRM

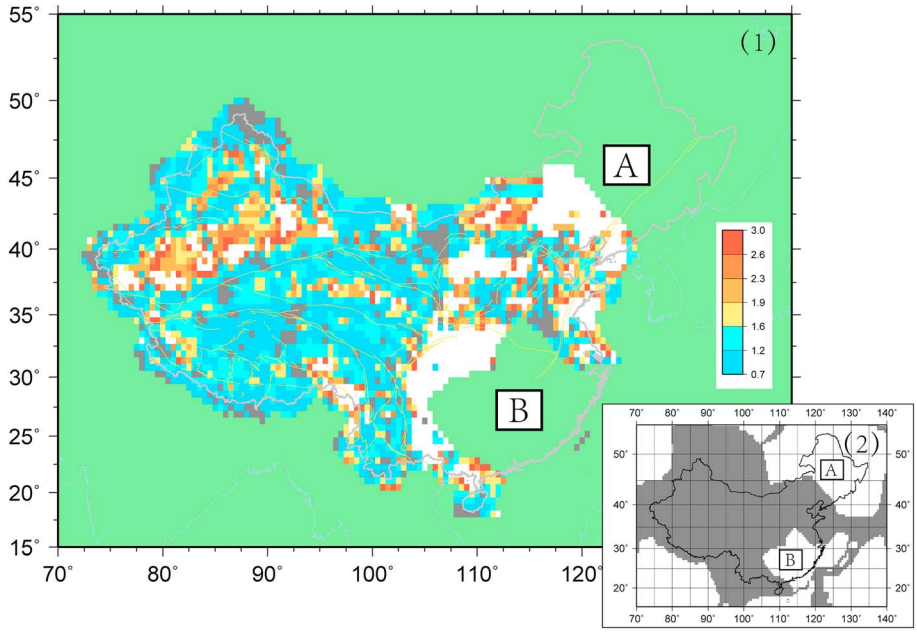


**Figure 11.** (1) Ratio of second invariant strain rate of this study to GSRM v2.1. The ratio higher than 3.0 and lower than 0.7 are shaded in white and gray respectively. Regions labeled as A and B are corresponding to the labeled regions in inset map. (2) Geometry setting in Global Strain Rate Model (GSRM) 2.1 of Kreemer et al. (2014), where the gray shading is outline of areas allowed to deform and the white areas were assumed to be rigid plates where no strain rates were calculated.

v2.1 by first interpolating the second invariant strain rate of each model into a common grid spacing (0.25° longitude by 0.25° latitude in dimension). We then calculate the ratio of the two models.

The result is shown in Figure 11. Overall the ratio falls between 0.7 and 1.6 in western China, where the Tibetan Plateau is located. However, a region with high ratios is seated around the Tarim basin. We attribute the high ratio in this region to the sparseness of GPS sites in the region (see Figure 1) and coarser spatial resolution setting used in our model. Thus, for the Tarim basin, even though strain rates in this region are low, because no GPS sites are deployed here, the strain rates will be poorly constrained and easily be affected by surrounding high strain rate regions, for example, the Altyn fault and Tianshan orogen. In eastern China, the majority of ratios are saturated indicating a poor fit (ratios higher than 3.0 are shaded in white). This saturation is due to the rigidity assumption in GSRM v2.1, where regions A and B in Figure 11 are assumed to be rigid and predict zero strain rates there. The disadvantage of this assumption is that to ensure the estimated strain rates are smoothly transitioned to zero from the deforming zones (gray area in inset map of Figure 11) to rigid zone, the modeled strain rates on the margins of deformation zones will be underestimated. Furthermore, if a deformed region is separated by two rigid zones, as in the case of eastern China, (1) the strain rates may be distorted if the angular velocity vectors of the surrounding rigid zones are not well determined and (2) the strain rates may be underestimated because they are forced to decrease to zero on both sides. Therefore, even though the rigidity assumption can dramatically reduce the computational burden when estimating the global strain rate model, we do not recommend imposing the rigidity constraint in a local area.

### 7.2. Implications for Seismic Hazards

Long-term forecasting of seismicity is an essential service that seismology provides to the global community (Bird & Kreemer, 2015). Geodetic strain rates provide an important constraint on expected seismic activity, but only after the strain rates are converted to appropriate (*tectonic* or *geodetic*) moment rates (Kreemer et al., 2014). To convert our newly derived geodetic strain rate results to a forecast of long-term average seismicity of mainland China, we follow the SHIFT (Seismic Hazard Inferred from Tectonics) hypothesis and algorithms detailed by Bird and Liu (2007) and Bird and Kreemer (2015). The major SHIFT hypothesis entails

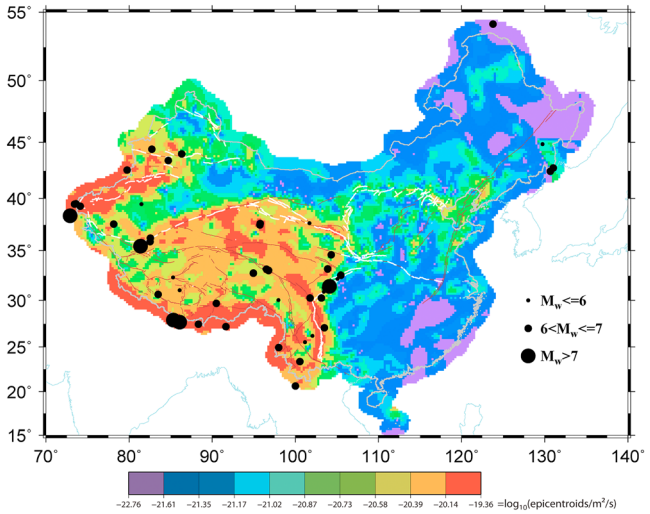


**Figure 12.** Common logarithm of the tectonic forecast of seismicity (in epicenters per square meter per second, including aftershocks) in the study area at or above threshold M 5.67 for years 2008 and after. The forecast was calibrated using the Global Centroid Moment Tensor catalog years 1997–2007, based on the necessary parameters determined by Bird and Kagan (2004), the PB2002 rigid-plate model of Bird (2003), and the plate-boundary assignment rules (model F) suggested by Bird and Kreemer (2015).

(1) the long-term seismicity along any tectonic fault can be approximately computed from its moment rate by using the frequency/magnitude relationship (e.g., Bird & Kagan, 2004) of the most comparable type of plate boundary (e.g., Bird & Liu, 2007) and (2) the long-term moment rate along any tectonic fault can be computed by using the strain rate tensor and mean coupled seismogenic thickness (i.e., dimensionless seismic coupling coefficient multiplied by seismogenic thickness) of the most comparable type of plate boundary (e.g., Bird & Kagan, 2004). In summary, our calculation is based on the PB2002 rigid-plate model developed by Bird (2003), plate-boundary assignment rules suggested by Bird and Kreemer (2015), and the other necessary parameters (coupled seismogenic thickness, spectral slope β, and corner magnitude) determined by Bird and Kagan (2004).

Figure 12 shows the logarithm of our forecast seismicity (including aftershocks) above threshold magnitude 5.67, which is the completeness threshold of Global Centroid Moment Tensor catalog (Dziewonski et al., 1981; Ekström et al., 2012) within the depth range of 0–70 km. The forecast was calibrated using the years 1977–2007 of the Global Centroid Moment Tensor catalog, leaving 10 years (2008–2017) for testing. During the test years, there were 59 shallow earthquakes at or above threshold of magnitude 5.767.

Overall, the regions with high forecasted seismicity rate are located at the central Tibetan Plateau, the Chuan-Dian region, the Tian Shan Orogen, and the North China Block. The Himalaya, the Xianshuihe-Xiaojiang fault system, the eastern Kunlun fault system, and the western Tian Shan orogen are the regions with highest forecasted seismicity rate.

Comparison between the seismicity rate and seismic magnitude, as shown in Figure 13, indicates the behavior of the forecast model. The red and green dotted lines represent the logarithm of seismicity rate valued at −20.4 and −20.87, corresponding to the zones with high seismicity rate shown in Figure 12. Earthquakes are located in the regions with forecasted seismicity rate higher than the median (green dotted line). Most of the earthquakes with magnitude larger than M7 (black dots) are located in the regions where high seismicity rates are forecasted (red dotted line). The largest discrepancy is at the location of the 2008 Wenchuan Mw 7.9 earthquake (red dot), which was unexpected. We note that although most devastating earthquakes have taken place in western China in the past 10 years (Figure 12), the forecasts of seismicity rates along the Zhangjiakou-Bohai and Tan-Lu fault belts in the north China block are still higher than the surrounding areas. Considering the high population density and occurrences of great historic earthquakes (Liu et al., 2007; Zhang et al., 2018), this work eludes to the need for more efforts towards seismic resiliency in these specific regions. It is also noteworthy that our calculation of seismic potential is inferred from the geodetic strain rate field with spatial resolution of only 0.4° × 0.4°. We can infer that with more GPS sites deployed in this region, especially in the intensely deformed areas, the strain rate pattern will be captured with more detail and thus the forecasted long-term seismicity may become higher.

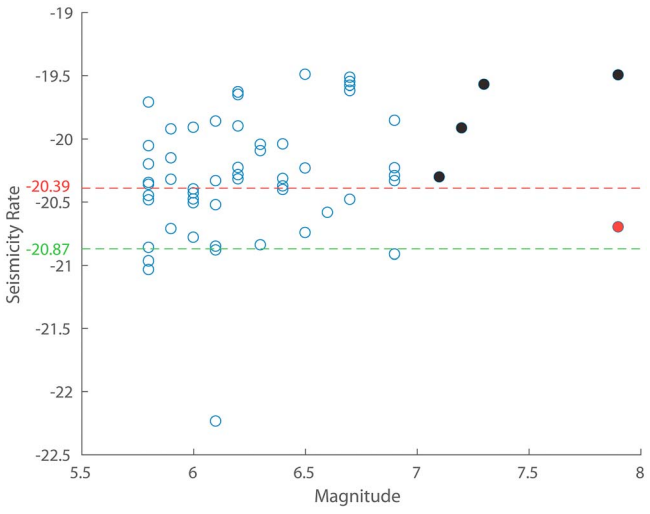


**Figure 13.** Forecast of seismicity rate versus the observed earthquakes of the years 2008–2017. The red and green dotted lines represent the logarithm of seismicity rate valued at −20.4 and −20.87, corresponding to the zones with median and high seismicity rate shown in (color scale of Figure 12). Generally, earthquakes are fallen into the regions where forecast seismicity rates are higher than the median (green dotted line). Most of the earthquakes with magnitude larger than M7 (black dots) are in the regions with high seismicity rate (red dotted line). The largest discrepancy is the 2008 Wenchuan Mw 7.9 earthquake (red dot), which was unexpected.

## 8. Conclusions

In this work we provide a quantitatively evaluated and validated tectonic GPS velocity solution, geodetic strain rate solution, and, following, estimated seismicity rate for mainland China. We calculate a tectonic GPS

velocity field by processing new and widely available continuous and episodic GPS data spanning 1999–2017. We implement a data editing scheme to account for 8 Mw ≥ 7 earthquakes to reduce the account for transient deformation. With the editing strategy, the average velocity uncertainties reach to ~0.28 and ~0.26 mm/year for the north and east component respectively. We combine this velocity solution with 10 other published sources to provide a new tectonic velocity solution for mainland China and its surrounding tectonic regions as a contribution to the broader geophysical community. We then used it to revise the geodetic strain rate and seismicity forecast model. We first determine an optimal mesh grid definition to be 0.4° × 0.4° based on Nyquist frequency method and checkerboard test. We then evaluate the tectonic strain rate model from both statistical and quantitative perspectives. The Bayesian factor and NRMS are close to unity, the GPS modeled strain rate is consistent with the peak average 2-D analytical model, and the majority of the earthquakes in the test catalog (2008–2017) are in regions with high seismicity rate forecasted by the calibrating earthquake catalog (1997–2007).

**Acknowledgments**
All velocity data supporting the conclusions of this paper are available as supporting information in GLOBK velocity format. NGL data with dois are referenced in the References section. We also provide the strain rate model and seismicity model as supporting information. We thank the Crustal Movement Observation Network of China and Hubei Earthquake Bureau for providing access to their data for publication in this manuscript. Rui Xu was funded by National Science Foundation of China 41704014 and supported by the science and technology innovation fund of Sichuan Earthquake Agency (201804). We thank Corné Kreemer and Peter Bird for insightful discussions about the strain rate and SHIFT codes.

## References

Allen, C. R., Zhuoli, L., Hong, Q., Xueze, W., Huawei, Z., & Weishi, H. (1991). Field study of a highly active fault zone: The Xianshuihe fault of southwestern China. *Geological Society of America Bulletin*, *103*(9), 1178–1199. https://doi.org/10.1130/0016-7606(1991)103<1178:FSOAHA>2.3.CO;2

Allmendinger, R. W., Reilinger, R., & Loveless, J. (2007). Strain and rotation rate from GPS in Tibet, Anatolia, and the Altiplano. *Tectonics*, *26*, TC3013. https://doi.org/10.1029/2006TC002030

Altamimi, Z., Métivier, L., & Collilieux, X. (2012). ITRF2008 plate motion model. *Journal of Geophysical Research*, *117*, B07402. https://doi.org/10.1029/2011JB008930

Armijo, R., Tapponnier, P., Mercier, J. L., & Han, T. L. (1986). Quaternary extension in southern Tibet: Field observations and tectonic implications. *Journal of Geophysical Research*, *91*, 13,803–13,872. https://doi.org/10.1029/JB091iB14p13803

Avouac, J. P., & Tapponnier, P. (1993). Kinematic model of active deformation in Central Asia. *Geophysical Research Letters*, *20*(10), 895–898. https://doi.org/10.1029/93GL00128

Banerjee, P., Bürgmann, R., Nagarajan, B., & Apel, E. (2008). Intraplate deformation of the Indian subcontinent. *Geophysical Research Letters*, *35*, L18301. https://doi.org/10.1029/2008GL035468

Beavan, J., & Haines, J. (2001). Contemporary horizontal velocity and strain rate fields of the Pacific-Australian plate boundary zone through New Zealand. *Journal of Geophysical Research*, *106*, 741–770. https://doi.org/10.1029/2000JB900302

Bendick, R., Bilham, R., Freymueller, J., Larson, K., & Yin, G. (2000). Geodetic evidence for a low slip rate in the Altyn Tagh fault system. *Nature*, *404*(6773), 69–72. https://doi.org/10.1038/35003555

Bird, P. (2003). An updated digital model of plate boundaries. *Geochemistry, Geophysics, Geosystems*, *4*(3), 1027. https://doi.org/10.1029/2001GC000252

Bird, P., & Kagan, Y. Y. (2004). Plate-tectonic analysis of shallow seismicity: Apparent boundary width, beta, corner magnitude, coupled lithosphere thickness, and coupling in seven tectonic settings. *Bulletin of the Seismological Society of America*, *94*(6), 2380–2399. plus electronic supplement, https://doi.org/10.1785/0120030107

Bird, P., & Kreemer, C. (2015). Revised tectonic forecast of global shallow seismicity based on version 2.1 of the Global Strain Rate Map. *Bulletin of the Seismological Society of America*, *105*(1), 152–166. https://doi.org/10.1785/0120140129

Bird, P., & Liu, Z. (2007). Seismic hazard inferred from tectonics: California in special issue on regional earthquake likelihood models. *Seismological Research Letters*, *78*(1), 37–48. https://doi.org/10.1785/gssrl.78.1.37

Blewitt, G., & Lavallée, D. (2002). Effect of annual signals on geodetic velocity. *Journal of Geophysical Research*, *107*(B7), 2010. https://doi.org/10.1029/2001JB000570

Bügmann, R., Kogan, M. G., Steblov, G. M., Hilley, G., Levin, V. E., & Apel, E. (2005). Interseismic coupling and asperity distribution along the Kamchatka subduction zone. *Journal of Geophysical Research*, *110*, B07405. https://doi.org/10.1029/2005JB003648

Chen, Q., Freymueller, J. T., Yang, Z., Xu, C., Jiang, W., Wang, Q., & Liu, J. (2004). Spatially variable extension in southern Tibet based on GPS measurements. *Journal of Geophysical Research*, *109*, B09401. https://doi.org/10.1029/2002JB002350

Deng, Q. D., Ran, Y. K., & Yang, X. P. (2007). *Map of Active Tectonics in China (1:4000000) (in Chinese)*. Beijing: Seismological Press.

Devachandra, M., Kundu, B., Catherine, J., Kumar, A., & Gahalaut, V. K. (2014). Global Positioning System (GPS) measurements of crustal deformation across the frontal eastern Himalayan syntaxis and seismic-hazard assessment. *Bulletin of the Seismological Society of America*, *104*(3), 1518–1524. https://doi.org/10.1785/0120130290

Dong, D.-N., Herring, T. A., & King, R. W. (1998). Estimating regional deformation from a combination of space and terrestrial geodetic data. *Journal of Geodesy*, *72*(4), 200–214. https://doi.org/10.1007/s001900050161

Dziewonski, A. M., Chou, T.-A., & Woodhouse, J. H. (1981). Determination of earthquake source parameters from waveform data for studies of global and regional seismicity. *Journal of Geophysical Research*, *86*, 2825–2852. https://doi.org/10.1029/JB086iB04p02825

Ekström, G., Nettles, M., & Dziewonski, A. M. (2012). The global CMT project 2004-2010: Centroid-moment tensors for 13,017 earthquakes. *Physics of the Earth and Planetary Interiors*, *200-201*, 1–9. https://doi.org/10.1016/j.pepi.2012.04.002

Elliott, J. R., Biggs, J., Parsons, B., & Wright, T. J. (2008). InSAR slip rate determination on the Altyn Tagh Fault, northern Tibet, in the presence of topographically correlated atmospheric delays. *Geophysical Research Letters*, *35*, L12309. https://doi.org/10.1029/2008GL033659

England, P., & Houseman, G. (1986). Finite strain calculations of continental deformation: 2. Comparison with the India-Asia collision zone. *Journal of Geophysical Research*, *91*(B3), 3664–3676.

Fielding, E. J., Sladen, A., Li, Z., Avouac, J. P., Bürgmann, R., & Ryder, I. (2013). Kinematic fault slip evolution source models of the 2008 M7. 9 Wenchuan earthquake in China from SAR interferometry, GPS and teleseismic analysis and implications for Longmen Shan tectonics. *Geophysical Journal International*, *194*(2), 1138–1166. https://doi.org/10.1093/gji/ggt155

Flesch, L. M., Haines, A. J., & Holt, W. E. (2001). Dynamics of the India-Eurasia collision zone. *Journal of Geophysical Research*, *106*(B8), 16,435–16,460. https://doi.org/10.1029/2001JB000208

Gahalaut, V. K., Kundu, B., Laishram, S. S., Catherine, J., Kumar, A., Singh, M. D., et al. (2013). Aseismic plate boundary in the Indo-Burmese wedge, northwest Sunda Arc. *Geology*, *41*(2), 235–238. https://doi.org/10.1130/G33771.1

Gan, W., Zhang, P., Shen, Z. K., Niu, Z., Wang, M., Wan, Y., et al. (2007). Present-day crustal motion within the Tibetan Plateau inferred from GPS measurements. *Journal of Geophysical Research*, *112*, B08416. https://doi.org/10.1029/2005JB004120

Ge, W. P., Molnar, P., Shen, Z. K., & Li, Q. (2015). Present-day crustal thinning in the southern and northern Tibetan Plateau revealed by GPS measurements. *Geophysical Research Letters*, *42*, 5227–5235. https://doi.org/10.1002/2015GL064347

Gilder, S. A., Leloup, P. H., Courtillot, V., Chen, Y., Coe, R. S., Zhao, X., et al. (1999). Tectonic evolution of the Tancheng-Lujiang (Tan-Lu) fault via Middle Triassic to Early Cenozoic paleomagnetic data. *Journal of Geophysical Research*, *104*(B7), 15,365–15,390. https://doi.org/10.1029/1999JB900123

Hackl, M., Malservisi, R., & Wdowinski, S. (2009). Strain rate patterns from dense GPS networks. *Natural Hazards and Earth System Sciences*, *9*(4), 1177–1187. https://doi.org/10.5194/nhess-9-1177-2009

Haines, A. J., & Holt, W. E. (1993). A procedure for obtaining the complete horizontal motions within zones of distributed deformation from the inversion of strain rate data. *Journal of Geophysical Research*, *98*, 12,057–12,082. https://doi.org/10.1029/93JB00892

Haines, A. J., Jackson, J. A., Holt, W. E., & Agnew, D. C. (1998). *Representing distributed deformation by continuous velocity fields*, Sci. Rep. 98/5 (p. 110). Lower Hutt, New Zealand: Institute of Geological and Nuclear Sciences.

He, J., Vernant, P., Chéry, J., Wang, W., Lu, S., Ku, W., et al. (2013). Nailing down the slip rate of the Altyn Tagh fault. *Geophysical Research Letters*, *40*, 5382–5386. https://doi.org/10.1002/2013GL057497

Hengl, T. (2006). Finding the right pixel size. *Computers & Geosciences*, *32*(9), 1283–1298. https://doi.org/10.1016/j.cageo.2005.11.008

Herring, T. A. (2003). *GLOBK: Global Kalman filter VLBI and GPS analysis program Version 10.1 Internal Memorandum*. Cambridge: Massachusetts Institute of Technology.

Herring, T. A., King R. W., Floyd M. A., & McClusky S. C. (2016). Introduction to GAMIT/GLOBK. Release 10.6. Massachusetts Institute of Technology. http;//geoweb.mit.edu/~simon/gtgt/Intro_GG.pdf

Herring, T. A., Melbourne, T. I., Murray, M. H., Floyd, M. A., Szeliga, W. M., King, R. W., et al. (2016). Plate boundary observatory and related networks: GPS data analysis methods and geodetic products. *Reviews of Geophysics*, *54*, 759–808. https://doi.org/10.1002/2016RG000529

Huang, M. H., Bürgmann, R., & Freed, A. M. (2014). Probing the lithospheric rheology across the eastern margin of the Tibetan Plateau. *Earth and Planetary Science Letters*, *396*, 88–96. https://doi.org/10.1016/j.epsl.2014.04.003

Ischuk, A., Bendick, R., Rybin, A., Molnar, P., Khan, S. F., Kuzikov, S., et al. (2013). Kinematics of the Pamir and Hindu Kush regions from GPS geodesy. *Journal of Geophysical Research: Solid Earth*, *118*, 2408–2416. https://doi.org/10.1002/jgrb.50185

Jouanne, F., Awan, A., Pêcher, A., Kausar, A. J., Mugnier, L., Khan, I., et al. (2014). Present-day deformation of northern Pakistan from Salt Ranges to Karakorum ranges. *Journal of Geophysical Research: Solid Earth*, *119*, 2487–2503. https://doi.org/10.1002/2013JB010776

Kreemer, C., Blewitt, G., & Klein, E. C. (2014). A geodetic plate motion and global strain rate model. *Geochemistry, Geophysics, Geosystems*, *15*, 3849–3889. https://doi.org/10.1002/2014GC005407

Li, H., Li, S., Song, X. D., Gong, M., Li, X., & Jia, J. (2012). Crustal and uppermost mantle velocity structure beneath northwestern China from seismic ambient noise tomography. *Geophysical Journal International*, *188*(1), 131–143. https://doi.org/10.1111/j.1365-246X.2011.05205.x

Li, Q., You, X., Yang, S., Du, R., Qiao, X., Zou, R., & Wang, Q. (2012). A precise velocity field of tectonic deformation in China as inferred from intensive GPS observations. *Science China Earth Sciences*, *55*(5), 695–698. https://doi.org/10.1007/s11430-012-4412-5

Li, S. P., Chen, G., & Li, J. W. (2015). Analysis of crustal deformation and strain characteristics in the Tianshan Mountains with least-squares collocation. *Solid Earth Discussions*, *7*(4), 3179–3197. https://doi.org/10.5194/sed-7-3179-2015

Liang, S., Gan, W., Shen, C., Xiao, G., Liu, J., Chen, W., et al. (2013). Three-dimensional velocity field of present-day crustal motion of the Tibetan Plateau derived from GPS measurements. *Journal of Geophysical Research: Solid Earth*, *118*, 5722–5732. https://doi.org/10.1002/2013JB010503

Liu, M., Yang, Y., Shen, Z., Wang, S., Wang, M., & Wan, Y. (2007). Active tectonics and intracontinental earthquakes in China: The kinematics an geodynamics, in Continental Intraplate Earthquakes: Science, Hazard, and Policy Issues, edited by S. Stein and S. Mazzotti. *Spec. Pap. Geol. Soc. Am.*, *425*, 209–318. https://doi.org/10.1130/2007.2425

Loveless, J. P., & Meade, B. J. (2010). Geodetic imaging of plate motions, slip rates, and partitioning of deformation in Japan. *Journal of Geophysical Research*, *115*, B02410. https://doi.org/10.1029/2008JB006248

Marone, C. J., Scholtz, C. H., & Bilham, R. (1991). On the mechanics of earthquake afterslip. *Journal of Geophysical Research*, *96*(B5), 8441–8452. https://doi.org/10.1029/91JB00275

Martone, M. (2014). Joint declaration of data citation principles–FINAL. *FORCE11*.

McCaffrey, R., Qamar, A. I., King, R. W., Wells, R., Khazaradze, G., Williams, C. A., et al. (2007). Fault locking, Block Rotation and Crustal Deformation in the Pacific Northwest. *Geophysical Journal International*, *169*(3), 1315–1340. https://doi.org/10.1111/j.1365-246X.2007.03371.x

McClusky, S., Balassanian, S., Barka, A., Demir, C., Ergintav, S., Georgiev, I., et al. (2000). Global Positioning System constraints on plate kinematics and dynamics in the eastern Mediterranean and Caucasus. *Journal of Geophysical Research*, *105*(B3), 5695–5719. https://doi.org/10.1029/1999JB900351

Meade, B. J., & Loveless, J. P. (2017). Block motion changes in Japan triggered by the 2011 great Tohoku earthquake. *Geochemistry, Geophysics, Geosystems*, *18*, 2459–2466. https://doi.org/10.1002/2017GC006983

Métois, M., Socquet, A., & Vigny, C. (2012). Interseismic coupling, segmentation and mechanical behavior of the central Chile subduction zone. *Journal of Geophysical Research*, *117*, B03406. https://doi.org/10.1029/2011JB008736

Mohadjer, S., Bendick, R., Ischuk, A., Kuzikov, S., Kostuk, A., Saydullaev, U., et al. (2010). Partitioning of India-Eurasia convergence in the Pamir-Hindu Kush from GPS measurements. *Geophysical Research Letters*, *37*, L04305. https://doi.org/10.1029/2009GL041737

Molnar, P. (1988). A review of geophysical constraints on the deep structure of the Tibetan Plateau, the Himalaya and the Karakoram, and their tectonic implications. *Philosophical Transactions of the Royal Society London*, *326*(1589), 33–88. https://doi.org/10.1098/rsta.1988.0080

Molnar, P., & Tapponnier, P. (1975). Cenozoic tectonics of Asia: Effects of a continental collision. *Science*, *189*(4201), 419–426. https://doi.org/10.1126/science.189.4201.419

Nur, A., & Mavko, G. (1974). Postseismic viscoelastic rebound. *Science*, *183*(4121), 204–206. https://doi.org/10.1126/science.183.4121.204

Qi, J., Zhou, X., Deng, R., & Zhang, K. (2008). Structural characteristics of the Tan-Lu fault zone in Cenozoic basins offshore the Bohai Sea. *Science in China Series D: Earth Sciences*, *51*(S2), 20–31. https://doi.org/10.1007/s11430-008-6013-x

Reilinger, R., McClusky, S., Vernant, P., Lawrence, S., Ergintav, S., Cakmak, R., et al. (2006). GPS constraints on continental deformation in the Africa-Arabia-Eurasia continental collision zone and implications for the dynamics of plate interactions. *Journal of Geophysical Research*, *111*(B5), B05411. https://doi.org/10.1029/2005JB004051

Riguzzi, F., Crespi, M., Devoti, R., Doglioni, C., Pietrantonio, G., & Pisani, A. R. (2012). Geodetic strain rate and earthquake size: New clues for seismic hazard studies. *Physics of the Earth and Planetary Interiors*, *206*, 67–75.

Royden, L. H., Burchfiel, B. C., King, R. W., Wang, E., Chen, Z., Shen, F., & Liu, Y. (1997). Surface deformation and lower crustal flow in eastern Tibet. *Science*, *276*(5313), 788–790. https://doi.org/10.1126/science.276.5313.788

Rui, X., & Stamps, D. S. (2016). Present-day kinematics of the eastern Tibetan Plateau and Sichuan Basin: Implications for lower crustal rheology. *Journal of Geophysical Research: Solid Earth*, *121*, 3846–3866. https://doi.org/10.1002/2016JB012839

Savage, J. C. (1990). Equivalent strike-slip earthquake cycles in half-space and lithosphere-asthenosphere Earth models. *Journal of Geophysical Research*, *95*(B4), 4873–4879. https://doi.org/10.1029/JB095iB04p04873

Savage, J. C., & Burford, R. O. (1973). Geodetic determination of relative plate motion in Central California. *Journal of Geophysical Research*, *78*, 832–845. https://doi.org/10.1029/JB078i005p00832

Schiffman, C., Bali, B. S., Szeliga, W., & Bilham, R. (2013). Seismic slip deficit in the Kashmir Himalaya from GPS observations. *Geophysical Research Letters*, *40*, 5642–5645. https://doi.org/10.1002/2013GL057700

Shen, Z. K., Sun, J., Zhang, P., Wan, Y., Wang, M., Bürgmann, R., et al. (2009). Slip maxima at fault junctions and rupturing of barriers during the 2008 Wenchuan earthquake. *Nature Geoscience*, *2*(10), 718–724. https://doi.org/10.1038/ngeo636

Smith, B., & Sandwell, D. (2003). Coulomb stress accumulation along the San Andreas fault system. *Journal of Geophysical Research*, *108*(B6), 2296. https://doi.org/10.1029/2002JB002136

Smith-Konter, B. R., Sandwell, D. T., & Shearer, P. (2011). Locking depths estimated from geodesy and seismology along the San Andreas Fault System: Implications for seismic moment release. *Journal of Geophysical Research*, *116*, B06401. https://doi.org/10.1029/2010JB008117

Tapponnier, P., Zhiqin, X., Roger, F., Meyer, B., Arnaud, N., Wittlinger, G., & Jingsui, Y. (2001). Oblique stepwise rise and growth of the Tibet Plateau. *Science*, *294*(5547), 1671–1677. https://doi.org/10.1126/science.105978

Tong, X., Sandwell, D. T., & Fialko, Y. (2010). Coseismic slip model of the 2008 Wenchuan earthquake derived from joint inversion of interferometric synthetic aperture radar, GPS, and field data. *Journal of Geophysical Research*, *115*, B04314. https://doi.org/10.1029/2009JB006625

Vernant, P., Bilham, R., Szeliga, W., Drupka, D., Kalita, S., Bhattacharyya, A. K., et al. (2014). Clockwise rotation of the Brahmaputra Valley relative to India: Tectonic convergence in the eastern Himalaya, Naga Hills, and Shillong Plateau. *Journal of Geophysical Research: Solid Earth*, *119*, 6558–6571. https://doi.org/10.1002/2014JB011196

Wang, H., Liu, M., Cao, J., Shen, X., & Zhang, G. (2011). Slip rates and seismic moment deficits on major active faults in mainland China. *Journal of Geophysical Research*, *116*, B02405. https://doi.org/10.1029/2010JB007821

Wang, H., & Wright, T. J. (2012). Satellite geodetic imaging reveals internal deformation of western Tibet. *Geophysical Research Letters*, *39*, L07303. https://doi.org/10.1029/2012GL051222

Wang, H., Wright, T. J., & Biggs, J. (2009). Interseismic slip rate of the northwestern Xianshuihe fault from InSAR data. *Geophysical Research Letters*, *36*, L03302. https://doi.org/10.1029/2008GL036560

Wang, J., Ye, Z. R., & He, J. K. (2008). Three-dimensional mechanical modeling of large-scale crustal deformation in China constrained by the GPS velocity field. *Tectonophysics*, *446*(1–4), 51–60. https://doi.org/10.1016/j.tecto.2007.11.006

Wang, M., Shen, Z. K., Niu, Z. J., Zhang, Z. S., Sun, H. R., Gan, W. J., et al. (2003). Present-day crustal movement of Chinese mainland and active block model (in Chinese). *Science in China(D)*, *33*(Suppl), 21–33.

Wang, Q., Zhang, P. Z., Freymuller, J., Bilham, R., Larson, K. M., Lai, X., et al. (2001). Present-day crustal deformation in China constrained by GPS measurement. *Science*, *294*(5542), 574–577. https://doi.org/10.1126/science.1063647

Wilkinson, M. D., Dumontier, M., Aalbersberg, I. J., Appleton, G., Axton, M., Baak, A., et al. (2016). The FAIR guiding principles for scientific data management and stewardship. Scientific data, 3.

Xu, X. W., Gui, Y. Y., Xi, H. T., & Kang, B. L. (2017). Seismo-geologicals signatures for identifying M ≥ 7 earthquake risk areas and their preliminary application in mainland China (in Chinese). *Seismology and Geology*, *39*(2), 219–275. https://doi.org/10.3969/j.issn.0253-4967.2017.02

Yang, Q. Y., Santosh, M., & Dong, G. (2014). Late Palaeoproterozoic post-collisional magmatism in the North China Craton: Geochemistry, zircon U–Pb geochronology, and Hf isotope of the pyroxenite–gabbro–diorite suite from Xinghe, Inner Mongolia. *International Geology Review*, *56*(8), 959–984. https://doi.org/10.1080/00206814.2014.908421

Yin, A., & Harrison, T. M. (2000). Geologic evolution of the Himalayan-Tibetan orogeny. *Annual Review of Earth and Planetary Sciences*, *28*(1), 211–280. https://doi.org/10.1146/annurev.earth.28.1.211

Yin, A., Kapp, P. A., Murphy, M. A., Manning, C. E., Mark Harrison, T., Grove, M., et al. (1999). Significant late Neogene east-west extension in northern Tibet. *Geology*, *27*(9), 787–790. https://doi.org/10.1130/0091-7613(1999)027<0787:SLNEWE>2.3.CO;2

Zeng, Y., Petersen, M. D., & Shen, Z. K. (2018). Earthquake potential in California-Nevada implied by correlation of strain rate and seismicity. *Geophysical Research Letters*, *45*(4), 1778–1785. https://doi.org/10.1002/2017GL075967

Zhang, P. Z., Deng, Q. D., Zhang, Z. Q., & Li, H. B. (2013). Active faults, earthquake hazards and associated geodynamic processes in continental China (in Chinese). *Scientia Sinica Terrae*, *43*, 1607–1620.

Zhang, P. Z., Shen, Z., Wang, M., Gan, W., Bürgmann, R., Molnar, P., et al. (2004). Continuous deformation of the Tibetan Plateau from global positioning system data. *Geology*, *32*(9), 809–812. https://doi.org/10.1130/G20554.1

Zhang, Y. G., Zheng, W. J., Wang, Y. J., Zhang, D. L., Tian, Y. T., Wang, M., et al. (2018). Contemporary deformation of the North China Plain from Global Positioning System data. *Geophysical Research Letters*, *45*(4), 1851–1859. https://doi.org/10.1002/2017GL076599

Zhang, Z. M., Liou, J. G., & Coleman, R. G. (1984). An outline of the plate tectonics of China. *Geological Society of America Bulletin*, *95*(3), 295–312. https://doi.org/10.1130/0016-7606(1984)95<295:AOOTPT>2.0.CO;2

Zhao, B., Huang, Y., Zhang, C., Wang, W., Tan, K., & Du, R. (2015). Crustal deformation on the Chinese mainland during 1998–2014 based on GPS data. *Geodesy and Geodynamics*, *6*(1), 7–15. https://doi.org/10.1016/j.geog.2014.12.006

Zheng, G., Wang, H., Wright, T. J., Lou, Y., Zhang, R., Zhang, W., et al. (2017). Crustal deformation in the India-Eurasia collision zone from 25 years of GPS measurements. *Journal of Geophysical Research: Solid Earth*, *122*, 9290–9312. https://doi.org/10.1002/2017JB014465

Zheng, Y. F., Wen, J. X., & Zhao, G. C. (2013). Introduction to tectonics of China. *Gondwana Research*, *23*(4), 1189–1206. https://doi.org/10.1016/j.gr.2012.10.001

Zhu, S., & Shi, Y. (2011). Estimation of GPS strain rate and its error analysis in the Chinese continent. *Journal of Asian Earth Sciences*, *40*(1), 351–362. https://doi.org/10.1016/j.jseaes.2010.06.007

Zubovich, A. V., Wang, X. Q., Scherba, Y. G., Schelochkov, G. G., Reilinger, R., Reigber, C., et al. (2010). GPS velocity field for the Tien Shan and surrounding regions. *Tectonics*, *29*, TC6014. https://doi.org/10.1029/2010TC002772